

Research paper

# Simulation of compound anchor intrusion in dry sand by a hybrid FEM+SPH method

Haozhou He<sup>a</sup>, Andras Karsai<sup>b</sup>, Bangyuan Liu<sup>c</sup>, Frank L. Hammond III<sup>c</sup>, Daniel I. Goldman<sup>b</sup>, Chloé Arson<sup>a,\*</sup>

<sup>a</sup> School of Civil and Environmental Engineering, Georgia Institute of Technology, Atlanta, GA, USA

<sup>b</sup> School of Physics, Georgia Institute of Technology, Atlanta, GA, USA

<sup>c</sup> School of Mechanical Engineering, Georgia Institute of Technology, Atlanta, GA, USA

## ARTICLE INFO

### Keywords:

Compound anchors  
Cohesionless granular medium  
Intrusion  
Smoothed Particle Hydrodynamics  
Finite Element Method  
Arching effects

## ABSTRACT

The intrusion of deformable compound anchors in dry sand is simulated by coupling the Finite Element Method (FEM) with Smoothed Particle Hydrodynamics (SPH). This novel approach can calculate granular flows at lower computational cost than SPH alone. The SPH and FEM domains interact through reaction forces calculated from balance equations and are assigned the same soil constitutive model (Drucker–Prager) and the same constitutive parameters (measured or calibrated). Experimental force–displacement curves are reproduced for penetration depths of 8 mm or more (respectively, 20 mm or more) for spike-shaped (respectively, fan-shaped) anchors with 1 to 6 blades. As the number of blades increases, simulations reveal that the granular flow under the anchor deviates from the vertical and that the horizontal granular flow transitions from orthoradial to radial. We interpret the strain field distribution as the result of soil arching, i.e., the transfer of stress from a yielding mass of soil onto adjoining stationary soil masses. Arching is fully active when the radial distance between blade end points is less than a critical length. In that case, the normal stress that acts on the compound anchor at a given depth reaches the normal stress that acts on a disk-shaped anchor of same radius. A single-blade anchor produces soil deformation and failure similar to Prandtl's foundation sliding model. Multiblade anchors produce a complex failure mechanism that combines sliding and arching.

## 1. Introduction

Intrusion, extrusion and drag of complex shaped objects have raised increasing attention among various scientific communities involved with the deployment of robots and structures for exploratory missions in submerged sediments (e.g., (Winter et al., 2014; Isava et al., 2016)) or extra-terrestrial regoliths (e.g., (Nagaoka et al., 2010; Kitamoto et al., 2012)). It is key to understand the fundamental mechanisms of anchoring, drag and lift in order to optimize burrowing and locomotion (Russell, 2011; Hosoi and Goldman, 2015; Naclerio et al., 2021; Martinez et al., 2021). Here, we investigate the potential cooperation mechanisms between the blades of compound anchors and we compare the performance of several designs for possible use in self-propelled devices. Propulsion forward generates shear forces backward and potential slip backward, which is to be avoided or minimized (Ma et al., 2020; Tao et al., 2020; Chen et al., 2022). We thus focus our study on the anchoring capacity of intruders of complex shapes for small penetration (slip) distances. We compare two compound shapes made of one to six fan-like components or one to six spike-like (sharp)

components. Little is known on the mechanisms that underpin the anchoring resistance of such compound shaped anchors because most studies focus on single-blade anchors or parallel single-blade anchors.

Plate anchors are typically used to resist pullout forces acting on structures such as retaining walls, or to provide propelling forces to underground machinery (Tian et al., 2014; Zhou et al., 2020). Single-component plate anchors were studied extensively both experimentally in Das (1980), Rowe and Davis (1982), Murray and Geddes (1987) and numerically in Merifield et al. (2001), Song et al. (2008) and Kumar and Kouzer (2008), but mostly for rectangular and circular shapes. A Finite Element (FE) analysis showed that the upward (counter gravity) movement of anchor plates leads to the formation of a quasi-rigid soil wedge, which moves upwards at the same velocity as that of the anchor plate (rigid body motion) (Kouzer and Kumar, 2009a). The movement of soil along sliding planes is indicative of soil yield. The transfer of stress from a yielding mass of soil onto adjoining stationary soil masses is known as “arching”. Arching effects translate into a change of stress orientation in the soil. The locus of isovalues of principal

\* Corresponding author.

E-mail address: [chloe.arson@ce.gatech.edu](mailto:chloe.arson@ce.gatech.edu) (C. Arson).

stresses is typically arch-shaped, hence the name. Hanna et al. (1972) and Geddes and Murray (1996) investigated arching effects between anchors through reduced-scale tests with groups of circular plates and square-shaped plate anchors, respectively. The effect of plate spacing on the vertical uplift anchoring capacity (i.e., pullout resistance) in cohesionless soil was theoretically examined through an upper bound limit analysis by Kouzer and Kumar (2009b), who showed that the force necessary to pull out a strip anchor (i.e., a rectangular plate, the length of which is at least 10 times its width) decreases when the distance to neighboring strip anchors decreases, and is lower than the vertical uplift resistance of an isolated strip anchor of the same dimensions and embedment ratio. In contrast to the pullout tests, vertical penetration tests conducted with horizontal rods by Pravin et al. showed that the total work per area over the depth of intrusion is maximum when the two rods are separated by a certain distance of the order of three particle diameters (Pravin et al., 2021). The effects of arching on reaction forces that develop during the intrusion of parallel disk anchors were investigated in Cruz and Caballero-Robledo (2016) and Agarwal et al. (2021), but to the authors' knowledge, arching effects between radial blades separated by an angular distance have never been investigated from the standpoint of anchoring capacity and granular flow. This is the objective of this paper, which focuses on a novel numerical approach to simulate intrusion in granular media.

The Finite Element Method (FEM) is routinely used to analyze and design plate soil anchoring systems (Naderi-Boldaji et al., 2012; Sano et al., 2013; Seo and Pelecanos, 2018; Jonak et al., 2020). Of note, the FEM allowed calculation of plate anchor capacity during pullout tests conducted with different loading directions, in both 2D and 3D (Merifield et al., 2005; Merifield and Sloan, 2006; Khatri and Kumar, 2009; Wang et al., 2010; Bhattacharya and Kumar, 2014; Feng et al., 2019a). However, excessive element distortion limits the efficiency and accuracy of FEM simulations. To overcome this issue, an Arbitrary Lagrangian Eulerian (ALE) formulation is often employed to let integration points move independently from the mesh frame. Mesh distortion problems can be alleviated by moving nodes, remeshing, and mapping the field variables from one mesh to the next. However, the applicability of the FEM is still limited for intrusion problems, because penetration of a granular medium (like soil) by a solid (like a cone) requires inserting a surface separation path within the soil body or defining symmetric boundary conditions (Huang et al., 2004; Liyanapathirana, 2009; Wang et al., 2015; Shen et al., 2018; Hakeem and Aubeny, 2019). It remains challenging to precisely capture the interaction mechanisms between an intruder and a granular material with the FEM.

The Discrete Element Method (DEM) offers an alternative to model the interactions between solids and particles. In the DEM, the granular medium is represented by particulate elements. The DEM consists in calculating the displacement and velocity fields of the particles as a result of their mutual force balances. Each particle is subjected to gravitational acceleration as well as elastic contact forces and dissipative normal and frictional forces from adjacent interacting particles. Many authors used the DEM to analyze cone penetration (e.g., (Calvetti and Nova, 2005; Butlanska et al., 2014; Gens et al., 2018; Khosravi et al., 2019)) and anchor pull-out (e.g., (Evans and Zhang, 2019; Liang et al., 2021)) but the DEM is computationally intensive. In many engineering scenarios, representing each soil grain by a particulate element is not feasible, and that is why a scaling factor is often used to allow simulation of large volumes of soil with a smaller number of large particulate elements (Gens et al., 2018; Evans and Zhang, 2019). The main inconvenience is that scaled DEM models must be re-calibrated each time the size of the particles is changed. In other words, such DEM models are scenario-specific. In addition, in most DEM packages, it is not straightforward to use non-ellipsoidal particle shapes and to customize the interaction laws (de Bono and McDowell, 2022).

There has been a growing interest in modeling the local interaction between anchors and soil with mesh-free techniques combined

with a continuum mechanics approach, such as the Material Point Method (MPM) (Liang et al., 2021) and the Smoothed Particle Hydrodynamics (SPH) method (Woo et al., 2015; Wu et al., 2019; Lu and Sonoda, 2021). Other MPM applications include the simulation of avalanches (Vriend et al., 2013), the modeling of cone penetration in soils (Ceccato et al., 2017) and the design of locomotion systems in granular media (Ortiz et al., 2019). SPH was used for solving solid-soil interaction problems beyond anchoring (Kulak and Bojanowski, 2011; Kulak and Schwer, 2012). Key to the MPM and SPH is the use of a continuum mechanics-based constitutive model for the granular medium, as opposed to interaction laws at particle contacts. The field variables (e.g., stress, strain, density) are calculated at material points that typically represent a Representative Elementary Volume (REV) of particles. Coupled governing equations can conveniently be solved to address complex engineering problems. For example, Bisht et al. used the MPM to simulate intrusion in saturated clays (Bisht et al., 2021). Despite its success in investigating local mechanisms of anchoring, the MPM has its limitations. First, the field variables are defined on a background grid that plays a role similar to the mesh in the FEM. In most MPM packages, the background grid is not updated once the simulation starts. Usually, it is necessary to model the whole soil domain with MPM particles of uniform size (Coetzee et al., 2005; Beuth, 2012; Martinelli and Galavi, 2021; Liang et al., 2021). It is also necessary to model a sufficiently large domain to avoid boundary effects and to use small particles to properly represent the interactions between the soil and the anchors. Modeling the whole soil domain with uniformly small particle elements yields high computational costs, and that is why many MPM studies treat 3D problems by solving pseudo-2D problems (e.g., plane stress or axis-symmetric conditions).

SPH, just like the MPM, is well-suited for large deformation problems of fluid-like materials. In SPH, the field variables at the material point are found by a kernel approximation method, which consists in calculating the weighted sum of the field variables of the neighboring particles over a certain range. SPH is attractive to model challenging geomechanical problems because of its truly mesh-free nature (Pastor et al., 2014; Wu et al., 2015; Nonoyama et al., 2015; Braun et al., 2017; Yang et al., 2020). Analyzing anchoring mechanisms with the SPH method presents two major advantages. First, the SPH method does not rely on a background grid, which makes it possible to simulate the soil far from the penetration zone with more efficient methods such as the FEM. Second, SPH methods have been implemented in the packages of popular commercial software such as ABAQUS and LS-DYNA, which offer powerful pre-processing and file exchange tools. This is a significant gain compared to the options available with the MPM to date, because pre- and post-processing of anchors of complex shapes is not trivial.

Based on these premises, we propose a novel approach to couple the SPH method with the FEM to simulate the penetration of compound anchors in dry sand. Results are benchmarked against measures taken during intrusion tests performed in the laboratory. Section 2 summarizes the experimental materials and methods. Section 3 presents the numerical approach adopted in this study to couple SPH and the FEM. The numerical model developed to simulate the intrusion experiments is described in detail in Section 4. The numerical and experimental force-displacement curves are compared in Section 5, in which the proposed SPH+FEM is further verified against analytical solutions of anchor bearing capacity. The dependence of the anchoring resistance to depth and the three-dimensional arching effects are analyzed in Section 6, and conclusions are drawn in Section 7.

## 2. Experimental intrusion tests

### 2.1. Materials employed

We used dry slightly polydisperse silica sand (300–850 micron) as our test substrate for the anchor penetration tests. We designed two

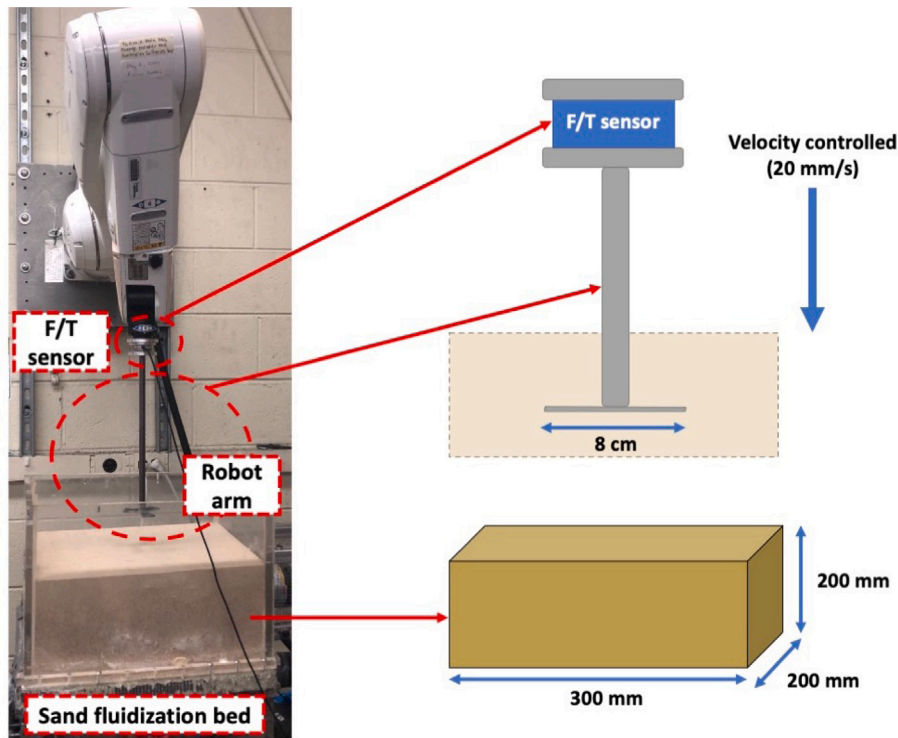


Fig. 1. Experimental set-up: robot arm and fluidized sand bed.

sets of anchors, the fan-shaped and sharp anchors, with the same 4 cm radius. Each set of anchors included different numbers of protruding features (either fans or blades), from one to six. These features were distributed equally in angle space. The anchor shapes were waterjet cut from a 410 AMS 5504 stainless steel sheet that was 2.29 mm thick (see Fig. 2). Each anchor was mounted to a 30 cm long, 1.27 cm thick steel rod, which was then attached to an ATI Mini40 six-axis force transducer. This transducer was attached to a DENSO VS087 robot arm which actuated the penetration and pullout motions.

## 2.2. Experimental set-up

Figs. 1 and 2 show the experimental set-up. The anchors were mounted on the robot arm that drove the anchors vertically to intrude the bed of sand at a constant speed, while the reaction force was measured by the ATI Mini40 transducer with an SI-80-4 calibration setting. To ensure sensor functionality and calibration, we placed plates of known weights at 2.27 kg and 4.54 kg as compressing loads on the sensor plate while mounted to the robot arm. The dimensions of the bed were 300 mm (L)  $\times$  200 mm (W)  $\times$  200 mm (H), with a maximum anchor intruding depth of 80 mm (test results beyond that depth were discarded because of potential boundary effects). Before each intrusion test, the bed was fluidized to reset the granular substrate to a loosely packed state. Fluidization was carried out by Toro leaf blowers pumping air into an acrylic expansion chamber which then diffused air through a plastic porous membrane. The airflow rate was manually selected to flow near the onset of bubbling fluidization across the surface of the entire bed. Fluidization proceeded for 15 s between each test. The penetration speed was set to 20 mm/s. Bending moments and reaction forces were recorded along the three principal directions. For each anchor shape, the intrusion test was repeated three times. For intrusion depths greater than 5 mm, the variability of the intrusion force was  $\pm 5\%$  in comparison to the intrusion force averaged among the three replicates (“mean intrusion force”), which was judged acceptable. The numerical model presented in the following was calibrated against the mean intrusion force for each anchor type.

## 3. The hybrid FEM+SPH method

### 3.1. Basic principles of the SPH method

The SPH method is a particle-based technique in which the positions of material points are tracked directly to allow calculation of large displacements. SPH was first developed by Gingold and Monaghan (1977) to simulate hydrodynamic flows. Later, SPH was applied for solving fluid mechanics and solid mechanics problems (Monaghan, 1992; Libersky et al., 1997; Gray et al., 2001). The theoretical framework of the SPH method is well documented in Gingold and Monaghan (1977), Monaghan (1992), Fuller (2010) and Bui and Nguyen (2021). In short, the simulation domain is discretized with a finite number of particle elements that are assigned field variables such as mass and velocity. The SPH algorithm solves the strong form of the Partial Differential Equations (PDEs) that govern the problem by means of a kernel approximation method that can be mathematically expressed as (Monaghan, 2005a,b, 2012):

$$f_{(x_i)} = \sum_{j=1}^N \frac{m_j}{\rho_i} W(x_i - x_j, h) \quad (1)$$

where the subscript  $i$  refers to the particle where the field variables are calculated and the subscripts  $j$  denote the particles around particle  $i$  within a distance of influence  $h$  (rate of influence intensity falling-off), as illustrated in Fig. 3.  $f_{(x_i)}$  is the approximation of the sought field variable at particle  $i$  and  $W(x_i - x_j, h)$  is a weight function, which depends on the inter-particle distances  $(x_i - x_j)$  and the distance of influence  $h$  (typically,  $W$  is an exponential decay function that vanishes at  $h$ ).  $m_j$  and  $\rho_j$  are respectively the mass and mass density of a particle  $j$  within the kernel area. The idea behind Eq. (1) is that in a continuum field represented by a set of material points, the field variable at material point  $i$  can be approximated by sampling from its neighboring material points  $j$  within a zone of influence of radius  $h$  (Fig. 3). The weight function  $W(x_i - x_j, h)$  is chosen such that the particles close to the center of the sampling kernel participate more in the approximation, while the particles located far from the kernel

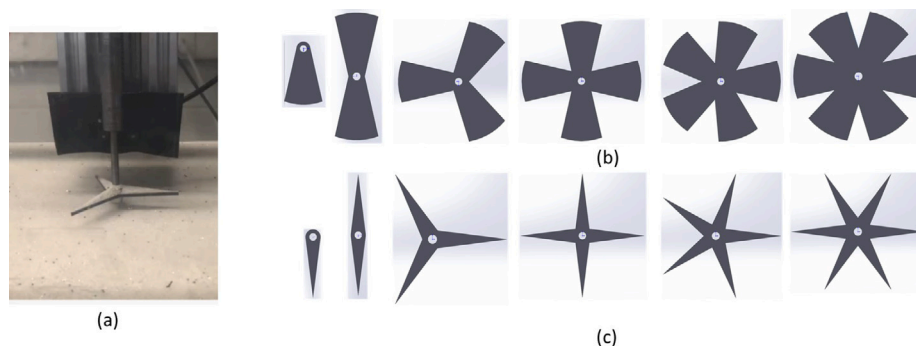


Fig. 2. The compound anchors used in the project. (a) Robot arm penetrating the fluidized silica bed with the three-blade sharp anchor. (b) Fan-shaped anchors, (c) Sharp anchors. All anchors were 4 cm in radius.

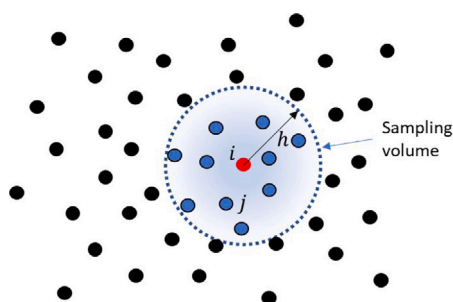


Fig. 3. The smooth kernel used in SPH to approximate the value at the  $i$ th particle by sampling a collection of  $N$  neighboring material points (noted  $j = 1 \dots N$ ) within a distance of influence  $h$ .

center have less impact on the approximation. The particles outside of the sampling area have no contribution to the approximation.

### 3.2. Coupling between SPH and FEM

Despite its broad applications, SPH is limited by its relatively high computational cost, which is significantly larger than that of grid-based simulations. Typically, in a small strain problem at constant density, the domain represented by one element in the FEM is discretized into a large number of particle elements in SPH, yielding a larger number of Degrees of Freedom (DOF). Additionally, the kernel approximation requires identifying the closest neighbors (that lie within the smooth kernel) for each particle at the beginning of each time increment. In the SPH method, three searching algorithms are usually implemented to find neighboring particles: all-pair search, tree search, and linked-list search. The computational complexity of all-pair search algorithm is  $O(N^2)$ , and that of the tree search and linked-list search algorithms is of order of  $O(N \log N)$  (Domínguez et al., 2011).

The accuracy and numerical stability of the SPH model is directly influenced by the kernel approximation process, which governs the calculation of the density of the granular medium. The mass of each SPH particle is constant through the calculation, so the density is derived from the number of SPH particles in a given volume. Anchor intrusion and pull-out lead to highly localized soil deformation and density changes, so fine SPH particles are needed near the penetration zone to capture the density change due to anchor intrusion. To ensure that the simulations results are reliable, it is necessary to reduce computational costs by other means than SPH particle enlargement alone.

We thus propose to use fine SPH particles close to the anchors, and to discretize the soil with the FEM in the far field, defined as the part of the soil domain that is subjected to small deformation (typically, the term small deformation is used for elastic deformation of the order of  $10^{-5}$  or less, and plastic small deformation of the order of  $10^{-3}$  or less). To solve the system of discretized equations, we use LS-DYNA. In our

hybrid SPH+FEM model, we replace 84% of the SPH particle elements by finite elements (Fig. 4). In addition to saving substantial amounts of computational time, the use of the FEM close to the outer boundaries of the domain makes it easier to apply boundary conditions, which is arguably an important challenge in SPH models (Vacondio et al., 2020). Although the prescribed boundary conditions can be directly applied to the SPH particles at boundaries, the kernel approximation functions for the nodes near the boundaries of the simulation domain are truncated, which may lead to inaccurate calculations. The solver must be adapted with *ad hoc* numerical treatments to avoid this issue (Bui et al., 2008a; Zhao et al., 2019). By contrast, the boundary conditions can be directly applied to FEM nodes at the boundaries of the simulation domain. Thus, our hybrid SPH+FEM simulation approach addresses issues of computational cost and boundary conditions that would be encountered with SPH alone.

Coupling of the SPH and FEM parts of the simulation domain consists of ensuring the continuity of both the displacement and velocity fields as well as the balance of forces at the SPH/FEM interface.

**Continuity of displacement and velocity fields.** The displacement or velocity of an SPH particle centroid, represented by  $f_{(x_i)}$  in Eq. (1), can be exported to nodes of the finite element domain. To build a model where SPH particle centroids are assigned the coordinates of finite element nodes, we initially meshed the entire soil domain with 8-node cubic finite elements and created a partition: a subdomain close to the anchors (to be replaced by SPH particles) and a subdomain close to the boundaries (to be left as is). Using MATLAB, the coordinates of the finite element nodes at the interface were assigned to SPH particle centroids. The duplicated nodes at the SPH soil–FEM soil interface were then merged, and the nodes of the finite elements within the high deformation zone (close to the anchor) were replaced with SPH particle elements. The two soil subdomains were thus modeled as a single unit of soil and the displacement and velocity fields were transferred through the SPH soil–FEM soil interface.

**Balance of forces.** To model the surface interaction between the FEM soil domain and the SPH particles that are not tied to the FEM/SPH soil interface, we used the penalty contact algorithm available in the LS-DYNA solver. As shown in Fig. 4, the basic idea of this approach is that the SPH particles can partially penetrate the surface of finite elements. At the beginning of each time step, if penetration is detected, the normal ( $F_N$ ) and tangential ( $F_T$ ) contact forces between the SPH particle and the finite element surface are calculated as:

$$\vec{F}_N = -kls\vec{n}, \quad F_T = \mu|F_N| \quad (2)$$

where  $k$  is the contact stiffness (which is an input parameter);  $s$  is the area of the face of the finite element;  $l$  is the penetration depth;  $\vec{n}$  indicates the direction normal to the contact surface;  $\mu$  is the friction coefficient.

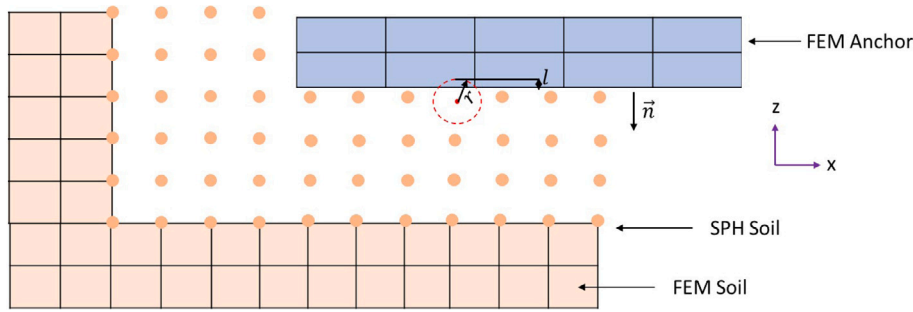


Fig. 4. Concept of the SPH+FEM hybrid model and the interaction between the SPH and FEM parts of the simulation domain (side view). The dots indicate the position of SPH particle centroids. The SPH particles (of radius  $r$ ) can penetrate the finite elements and the interpenetration distance is used to calculate the reaction forces at the anchor/soil interface and at the FEM/SPH soil interface, except for the SPH particles adjacent to the soil FEM domain, which are tied at their centroid to the nodes of the finite elements at the FEM/SPH soil interface.

#### 4. SPH+FEM model of compound anchor intrusion

##### 4.1. Geometry, interfaces and boundary conditions

The simulations were run on a super computer platform with 4 CPUs  $\times$  64 Cores. The system cut-off time of each simulation was 48 h. The setup of the numerical model, illustrated in Fig. 5, replicated the experimental conditions described in Section 2. The hybrid SPH/FEM approach described in Section 3 was used to model the soil. Anchors were modeled with the FEM, using the same shapes and dimensions as in the experiments. Taking advantage of the symmetry of the intrusion problems at stake, we only modeled half of the soil container. The dimensions of the half soil domain in the numerical model were 320 mm ( $L$ )  $\times$  160 mm ( $W$ )  $\times$  140 mm ( $H$ ), in which the SPH half-domain had dimensions 160 mm ( $L$ )  $\times$  80 mm ( $W$ )  $\times$  90 mm ( $H$ ). The lateral dimensions ( $L$  and  $W$  respectively) of the numerical soil domain (320 mm and 320 mm respectively) were larger than in the experiments (300 mm and 200 mm respectively): this was to avoid boundary effects such as extra confinement caused by lateral constraints. The height ( $H$ ) of the simulation domain (140 mm) was smaller than in the experiments (200 mm). This choice was a compromise between accuracy and computational cost, since a strict 48 h cut-off was applied on the super computers used in this study. We calibrated the domain size through several simulation campaigns in which we checked the boundary effects. The simulation domain size and the SPH subdomain dimensions adopted here avoided severe oscillations of the reaction curve in the early stages of the intrusion tests, suppressed SPH particle ejection, ensured smooth stress and displacement gradients at the FEM/SPH soil interface and yielded negligible deformation at the outer boundaries for the penetration depths under study (0–20 mm). On the plane of symmetry, the displacement in the  $y$ -direction and the shear stresses were set to 0. On the other lateral boundaries, the horizontal displacements and the vertical shear stress were fixed to 0. The displacements were fixed in all directions at the bottom boundary. The top boundary was free of stress. In each simulation, the anchor was pushed into the soil at a constant speed of 20 mm/s as in the experiments. The timestep lengths were automatically calculated by the solver. The vertical displacement of the anchor was controlled by the nodes attached to the loading axis, to mimic the connection between the loading rod and the anchor blades in the laboratory setup. Such a control of the imposed displacements allows simulation of blade bending if this were relevant (here, the blades are so stiff compared to the intruded granular medium that the deformation of the blades is negligible in our simulations).

The soil domain was evenly meshed with 8-node cubic solid finite elements and SPH particle elements. We calibrated the size of the SPH particles iteratively. For a particle radius of 5 mm, it was impossible to capture granular flow between the anchor blades, the width of which was in the same order of magnitude as the SPH particle size close to

the loading axis (around 10 mm). The reaction curves obtained for smaller particle sizes were similar when the particles had a radius  $r$  of 3 mm or less. The smaller the SPH particles, the smoother the reaction curve, but no major difference in trend or order of magnitude was noted between the results obtained with  $r = 1$  mm,  $r = 2$  mm and  $r = 3$  mm. It was also noted by other authors that increasing the SPH domain resolution beyond a certain point only helps smoothing the results, with marginal accuracy improvements (Korzani et al., 2017; Sasson et al., 2016). Simulations with  $r = 1$  mm allowed achieving a penetration depth of 10 mm or less before the cut off time of 48 h, which was not suitable for our study. Thus, we used  $r = 2$  mm. In total, 152,766 SPH particles and 6528 FEM elements were used to discretize the soil domain. In each simulation, the anchor was meshed with 8-node finite elements, using a seed density of 1 mm.

In agreement with the experiments, the anchor finite elements were assigned a purely linear elastic constitutive model with material properties typical of stainless steel: mass density  $\rho = 7500$  kg/m<sup>3</sup>, elastic modulus  $E = 200$  GPa, Poisson's ratio  $\nu = 0.26$ . The contact between the anchor (FEM) and the soil (SPH) was governed by Eq. (2) and the friction coefficient of the soil–anchor interface was set to 0.25 as in the DEM intrusion simulation conducted by Feng et al. (2019b), who used similar materials in their study. The SPH particles adjacent to the FEM soil domain were tied at their centroid to the finite element nodes at the FEM/SPH soil interface (see Section 3.2). The other SPH particles (inside the SPH domain) interacted with each other and with the FEM soil domain through the contact law given in Eq. (2), with a friction coefficient  $\mu = \tan \phi$ , where  $\phi$  is the internal friction angle of the sand.

##### 4.2. Soil constitutive model

We assigned the Soil and Crushable Foam (SCF) model available in LS-DYNA to the soil for both the FEM and SPH domains. The constitutive parameters of the SCF model can be chosen to match those of the Drucker Prager (DP) model. This is convenient, because the DP model was successfully used to simulate the interaction between intruders and dry granular media in many studies (e.g., Agarwal et al., 2019), and because the parameters of the DP model can be related to soil properties that can be measured in the laboratory (such as the friction angle and the cohesion coefficient). In this section, we explain how we calculated the parameters of the SCF model based on laboratory measurements.

We note  $p$  the mean stress:  $p = (\sigma_1 + \sigma_2 + \sigma_3)/3$  where  $\sigma_1$ ,  $\sigma_2$  and  $\sigma_3$  are the principal stress values. We note  $s$  the deviatoric stress, defined as  $s = \sigma - p\delta$ , where  $\sigma$  is Cauchy stress tensor and  $\delta$  is the second-order identity tensor. The yield criterion of the SCF model is described in terms of the mean stress and the second invariant of the deviatoric stress  $J_2 = \frac{1}{2} s : s$ , as follows:

$$J_2 = a_0 + a_1 p + a_2 p^2 \quad (3)$$

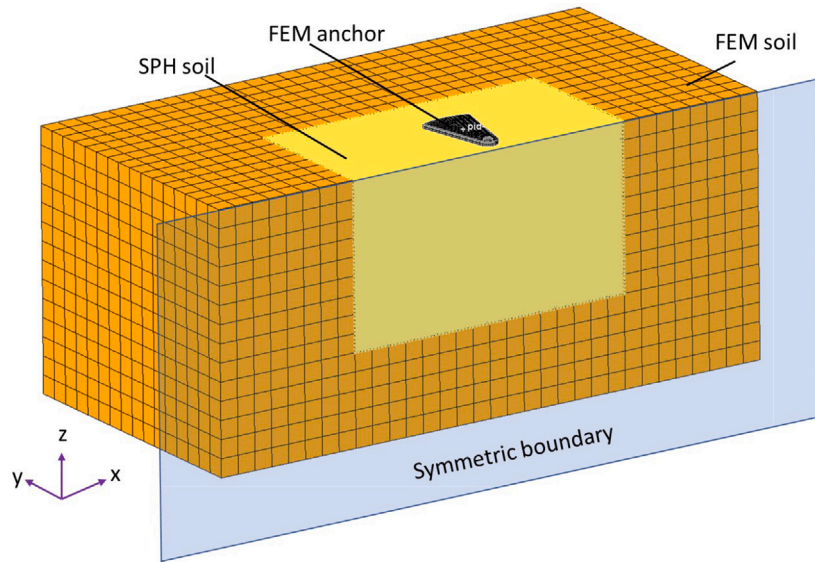


Fig. 5. The SPH/FEM hybrid model strategy. Dimensions of the half simulation domain: 320 mm (L) × 160 mm (W) × 140 mm (H). Size of the SPH zone in that domain: 160 mm (L) × 80 mm (W) × 90 mm (H).

where  $a_0, a_1, a_2$  are constitutive parameters. The first invariant of the stress tensor,  $I_1$ , is defined as  $I_1 = \sigma_1 + \sigma_2 + \sigma_3 = 3p$ . Introducing  $I_1$  in Eq. (3), one gets:

$$J_2 = a_2 \frac{I_1^2}{9} + a_1 \frac{I_1}{3} + a_0 \quad (4)$$

The DP yield criterion is expressed as:

$$\sqrt{J_2} = \alpha I_1 - k \quad (5)$$

where  $\alpha$  and  $k$  are constitutive parameters. Taking the square of both sides of Eq. (5):

$$J_2 = \alpha^2 I_1^2 - 2k\alpha I_1 + k^2 \quad (6)$$

We find the parameters of the SCF model by subtracting Eq. (6) from Eq. (4) and by noticing that each coefficient multiplying a stress term must be zero. We obtain:  $a_2 = 9\alpha^2, a_1 = -6k\alpha$  and  $a_0 = k^2$ .

We use the DP yield surface that circumscribes the Mohr–Coulomb (MC) yield surface of the soil, because that way, the two surfaces match at the compression corners (instead of the extension corners if the DP yield surface is inscribed in the MC yield surface). This choice was judged appropriate to simulate soil in compression during the anchor intrusion. The parameters of the circumscribed DP yield surface are (Alejano and Bobet, 2012):

$$\alpha = \frac{2 \sin \phi}{\sqrt{3(3 - \sin \phi)}} \quad (7)$$

$$k = \frac{6c \cos \phi}{\sqrt{3(3 - \sin \phi)}} \quad (8)$$

where  $c$  is the cohesion and  $\phi$  is the friction angle. The dry silica sand used in the experiments has no cohesion, i.e.  $c = 0$ , which implies that  $k = 0$ , and so,  $a_0 = a_1 = 0$ . In the absence of intrusion data on the internal friction angle of the substrate used in the intrusion tests, we assumed that the friction angle of the sand tested in the laboratory was equal to the angle of repose, which was found to be  $35^\circ$ . This gives  $\alpha \approx 0.2730$  and so  $a_2 \approx 0.671$ .

The density of the substrate was set to  $1650 \text{ kg/m}^3$ , which corresponds to the value of the substrate density measured experimentally. The values of the bulk modulus  $K$  and the shear modulus  $G$  of the silica sand were used as fitting parameters. We initially set  $K$  and  $G$  to values reported in Kulak and Schwer (2012) for other granular materials. We further calibrated  $K$  and  $G$  by trial and error, to match the force–displacement curves obtained experimentally for the 3-fan and 4-fan

anchors (see Section 5). The calibrated values are  $K = 4 \text{ MPa}$  and  $G = 13.6 \text{ kPa}$ .

## 5. Validation of the numerical model

### 5.1. Comparison to experiments

The values of the bulk and shear moduli of the sand were first calibrated to ensure that the proposed SPH+FEM model could predict the force–displacement curves obtained experimentally for 3-fan and 4-fan anchors. The other cases (1–6 sharp anchor blades, 1-fan, 2-fan, 5-fan and 6-fan anchors) were then run to validate the model predictions against the experimental force–displacement curves. In the simulations, the initial position of the anchor was 2 mm above the soil surface. We plotted the force–displacement curves for displacements greater than 2 mm, i.e., for the part of the simulation when the anchor was in contact with the soil. Fig. 6 shows that the vertical intrusion reaction force calculated numerically matches that obtained experimentally for both the 3-fan and 4-fan anchors, until the intrusion depth reaches about 30 mm. At larger depths, we observed that non-negligible shear stress was generated in the soil, close to the SPH/FEM interface, despite the continuity of the displacement field at that interface. The mobilization of the SPH domain eventually caused distortion of FEM soil domain. We expect that deeper intrusion could be simulated with more accuracy if the FEM soil domain below the anchor was replaced by SPH particles, but this solution would significantly increase the computational cost.

We now validate the model (calibrated for the 3-fan and 4-fan anchor systems) for the other compound anchors at similar intrusion depths. For fan-shaped anchors, the excessive distortion of the FEM mesh below the anchor system led to discrepancies between the experimental and numerical curves that started occurring at depths around 30 mm. Since the main objective of this study is to predict anchoring resistance of compound blades, we focus our study on small anchor displacements, which can be viewed as small slip displacements (backward) if the compound anchor was mounted on a self-propelled robot (moving forward). In the following results, we restrict our analyses to intrusion depths of 0–20 mm. The model presented in Fig. 5 allowed simulation of intrusion up to depths of 20 mm–40 mm for fan-shaped anchor systems and 8 mm–15 mm for sharp anchors within the 48-h cut-off time. These are larger displacements than expected at maximum bearing capacity for a tree-root-shaped anchor system (Mallett, 2019) which, with dimensions of same order of magnitude as the compound

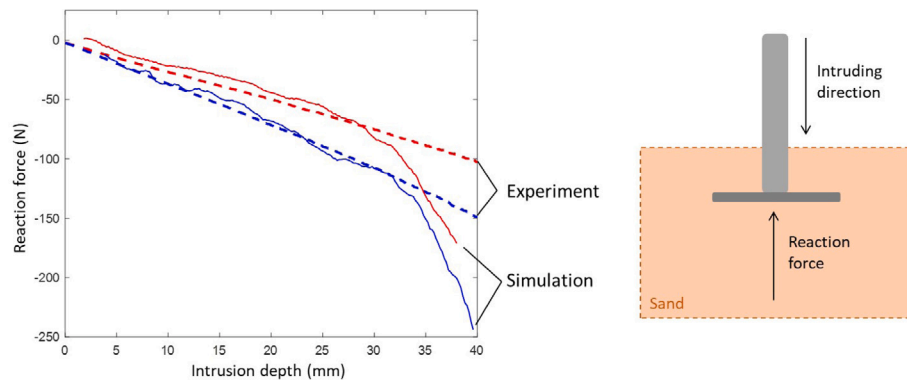


Fig. 6. Vertical intrusion reaction force curves for the 3-fan (in red) and 4-fan anchors (in blue). The numerical predictions match the experimental measures up to a depth of 30 mm.

blade systems tested here, achieves maximum bearing capacity for pullout displacements of 2.5 mm (0.1 in) and loses more than half of the maximum bearing capacity when the displacement reaches 5.0 mm (0.2 in).

Fig. 7 shows the intrusion depth/reaction force curves obtained experimentally and numerically. We focus on the performance of the numerical model to match the experimental curves for intrusions up to 20 mm depth. The numerical curves follow the linear experimental curves in trend and average for fan-shaped and sharp anchor systems with up to four blades, as well as for the 5-fan anchor. However, the simulated responses of the 6-fan, 6-sharp and 5-sharp anchor systems exhibit oscillations. The non-linearity observed in the 6-fan model is due to jamming followed by abrupt penetration at the beginning of the intrusion, which can be explained by the relatively large size of the SPH particles in comparison to the radial distance available for particulate flow between the blades (see Section 6). Interestingly, the numerical force–displacement curve for the 6-fan anchor matches the experimental one when the intrusion depth exceeds 7 mm. For the sharp anchors, the jumps observed in the force/displacement curves obtained numerically correspond to abrupt displacements of the spikes cutting through the SPH particles and producing free boundaries in the SPH domain above and below the anchor blades. The average width of the sharp blades is of the same order of magnitude as the SPH particle size, so the formation of free boundaries under the sharp blades creates an intermittent reaction force, which translates into oscillations in the force–depth curves. These oscillations are only seen for 5 and 6 blades, which we attribute to jamming induced by the confinement produced by adjacent blades. The mechanical processes of granular flow and soil deformation are explained in detail in Section 6.

Overall, the FEM+SPH model captures the linear evolution of the reaction force with the intrusion depth for compound anchors with four blades or less. For anchors with 5 and 6 blades, the model predicts the experimental intrusion force–displacement curve on average. Using smaller SPH particles should reduce the oscillations that occur because of intermittent reactions under the blades, and should increase the accuracy of the model. However, the computational cost is prohibitive. Based on these benchmark results, we now focus on the mechanical processes that explain the differences in the reaction/depth curves of the 12 anchor designs under study.

### 5.2. Analytical verification for a single-fan anchor

The velocity field in the soil domain at several stages of the intrusion by a 1-fan anchor is shown in Fig. 8. Once the anchor reaches a depth of 2 mm, a constant soil volume moves as a pseudo-rigid body under the anchor. The frictional resistance along the surface of this soil volume increases with the stress normal to the volume surface, and the normal stress itself increases linearly with depth. This explains why for

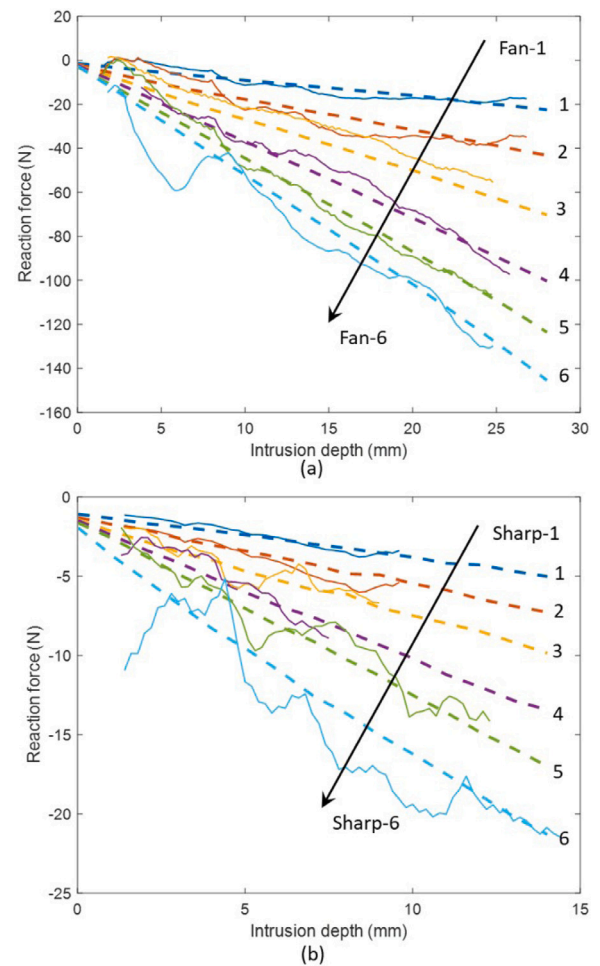


Fig. 7. Comparison of the force/intrusion curves obtained numerically with those obtained experimentally: (a) fan-shaped anchors; (b) spike-shaped (sharp) anchors. Dash lines are experimental results, solid lines are simulation results.

depths of 20 mm or less, the intrusion resistance increases linearly, in agreement with the experimental observations.

To check our interpretation of the linear response of the 1-fan intruder, we analyze the problem with a theoretical model of soil passive resistance. We use Terzaghi's formula (Terzaghi, 1943), which is an extension of the model of shallow failure mechanism proposed by Prandtl for calculating the bearing capacity of a strip foundation. The

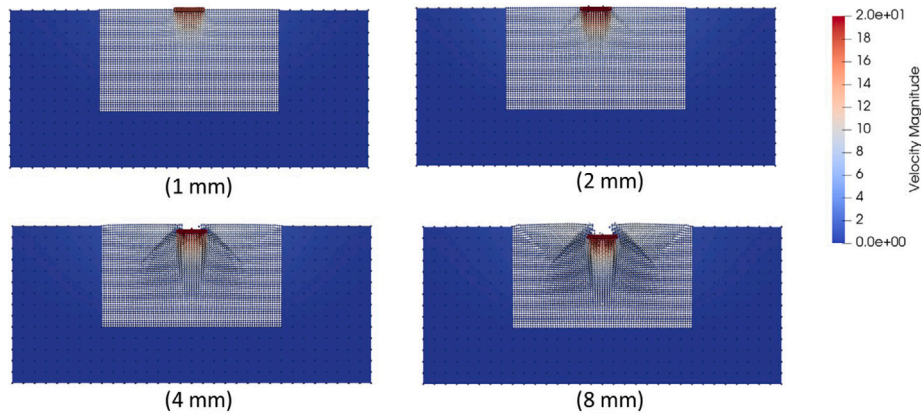


Fig. 8. The field of the norm of the soil velocity around a 1-fan anchor (cross-sectional view at mid-length of the blade) at several intrusion depths (SPH+FEM calculations). A constant soil volume moves as a rigid body under the anchor.

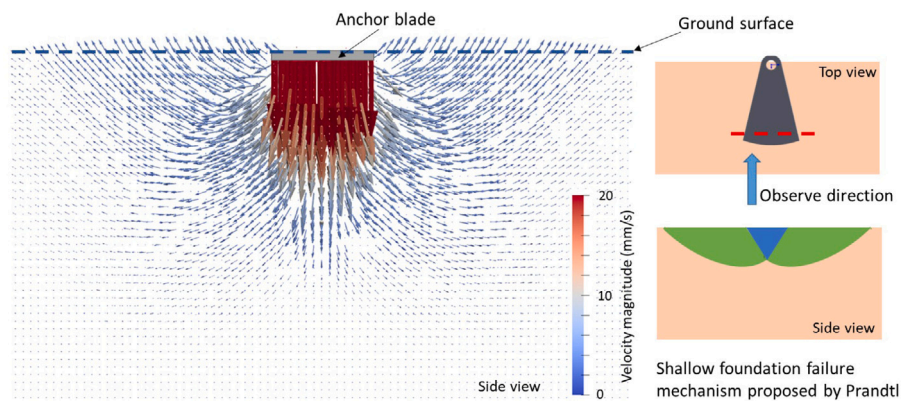


Fig. 9. The velocity field calculated in the SPH domain for a 1-fan anchor at an intrusion depth of 2 mm in comparison with the shallow foundation failure mechanism proposed by Prandtl.

analogy between the soil failure mechanisms under a single-fan anchor and under a strip foundation is illustrated in Fig. 9.

Terzaghi’s shallow foundation bearing capacity for a strip footing is written as:

$$q_{ult} = c N_c + \gamma' D N_q + 0.5 \gamma' B N_{\gamma'} \tag{9}$$

where  $c$  is the effective cohesion strength ( $c = 0$  for the silica sand used in this study),  $\gamma'$  is the effective weight per unit volume of the soil (here,  $\gamma' = 16.5 \text{ kN/m}^3$ ),  $B$  is the width of the strip (here, width of the 1-fan anchor at about half of the length:  $B = 15 \text{ mm}$ ) and  $D$  is the depth of the bottom face of the foundation. Here, the foundation length is the same as that of the 1-fan anchor ( $L = 40 \text{ mm}$ ). The term  $c N_c$  represents the bearing capacity due to the shear stress that develops along the sliding planes on the sides of the soil wedge below the foundation (represented in blue in Fig. 9). The term  $\gamma' D N_q$  represents the bearing capacity due to the weight of the upper layers of the sliding zones (represented in green in Fig. 9), which prevents the soil zones from sliding outward and thus impedes foundation settlement. The term  $0.5 \gamma' B N_{\gamma'}$  represents the passive resistance of the soil wedge under the foundation (illustrated in blue in Fig. 9).

Here, we calculate the bearing capacity of the strip foundation at several depths, and we compare it to the intrusion resistance of the 1-fan anchor at the same depths. The three factors  $N_c$ ,  $N_q$ , and  $N_{\gamma'}$  are related to the shear strength properties of the soil, the depth of the footing, and the overburden vertical stress respectively, as follows (Das and Larbi-Cherif, 1983; Coduto et al., 2001; Tezcan et al., 2006):

$$N_c = \frac{N_q - 1}{\tan \phi} \text{ for } \phi > 0 \tag{10}$$

$$N_q = \frac{e^{2\pi(0.75 - \phi/360)\tan \phi}}{2 \cos^2(45 + \phi/2)} \tag{11}$$

$$N_{\gamma'} = \frac{2(N_q + 1) \tan \phi}{1 + 0.4 \sin 4\phi} \tag{12}$$

where  $\phi = 35^\circ$  is the internal friction angle of the silica sand under study, which gives  $N_q = 41.5$  and  $N_{\gamma'} = 47.3$  ( $N_c$  is not needed since  $c = 0$  in this study). Using Eqs. (9)–(12), we find that the bearing capacity of a strip footing that has similar dimensions as those of the 1-fan anchor is a linear function of depth, as shown in Fig. 10. Note that in Terzaghi’s formula, the reaction force is not zero at the free surface (where  $D = 0$ ) because of the passive resistance of the soil (term  $0.5 \gamma' B N_{\gamma'}$ ). At a given depth, the difference between the intrusion reaction of the 1-fan anchor and the maximum force that a strip footing can bear can be attributed to the difference in shape (fan vs. strip). Soil failure observed under a 1-fan anchor can thus be qualitatively explained by the same failure mechanism as that of a strip foundation. In Section 6, we analyze the mechanisms that explain granular flow, soil deformation and soil failure during the intrusion of compound anchors with fan-shaped and spike-shaped blades.

## 6. Micromechanical analyses

### 6.1. Effect of angular spacing on the anchoring force: anchor cooperation

Two plate anchors set parallel to each other “cooperate” to generate more intrusion resistance than expected by summing the intrusion resistance forces of the two individual anchors if the spacing between the two lies within a range that depends on the grain size (Cruz and Caballero-Robledo, 2016; Pravin et al., 2021; Agarwal et al., 2021).



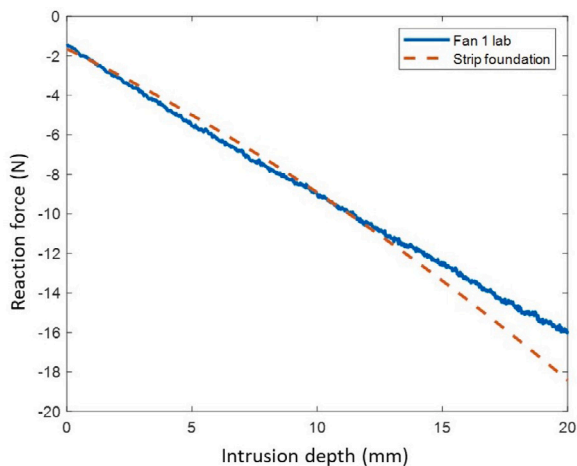


Fig. 10. Comparison of the reaction curve obtained experimentally for a one-fan anchor experiment to the reaction curve obtained with Terzaghi's formula for a strip foundation of length 40 mm and width 15 mm.

We hypothesize that the “cooperation” observed in the simulations is due to arching, i.e., the process by which stress is transferred from a yielding mass of soil onto adjoining stationary soil masses. Here, we aim to understand the response of anchor blades that are separated by angular distances and investigate the conditions in which arching effects might contribute to the intrusion resistance.

Fig. 11.a shows that the intrusion resistance increases with the number of fan-shaped blades for depths of 0–20 mm in the experiments. This is expected, since the surface area of the compound anchor increases with the number of blades. Interestingly, the force increases more slowly, and linearly, for 4 blades and more. Fig. 11b shows how the average normal stress that acts on the compound anchor (defined as the intrusion resistance divided by the surface area of the blades) varies with the number of fan-shaped blades. The shape of the compound anchor does not influence the magnitude of the normal stress at an intrusion depth of 5 mm. For depths greater than 5 mm, the normal stress on the anchor increases with the number of blades up to 4 blades. Increasing the number of blades above 4 does not increase the normal stress on the compound anchor in spite of the increase of reaction force, which means that the intrusion resistance is not only generated by the reaction at the soil/blade interfaces, but also, by the soil in between. This observation suggests that arching occurs in the soil surrounding compound anchor systems with 4, 5 and 6 fan-shaped blades, and implies that if the blades are regularly spaced, decreasing the number of blades from 6 to 5 or 4 does not increase the risk of blade rupture.

For the sake of comparison, we simulated an intrusion test at 20 mm/s with a disk-shaped anchor of same radius as that of the compound anchors (40 mm), with the same model parameters as those described for the simulations of the experiments in Section 4. We found that at a depth of 20 mm, the total reaction force on the disk was 130 N. The corresponding normal stress on the disk was 25.8 kPa, which is the same normal stress  $\pm 3\%$  as the average normal stress exerted on the fan-shaped anchors with 4, 5 and 6 blades (see Fig. 11b). This observation indicates that the normal stress on the anchor “saturates” at 4 blades: the average normal stress reaches the average normal stress that would be exerted on a disk that forms the convex hull of the anchor for four blades, and does not exceed that value when the number of blades is increased. Visualizations of granular flow around the fan-shaped and disk-shaped anchors (presented in Section 6.2) confirm this hypothesis of “anchor cooperation by normal stress saturation”.

Fig. 12.a shows that intrusion resistance increases non-linearly with the number of sharp blades for depths of 0–20 mm in the experiments. The average normal stress increases with the number of sharp blades

as more blades impose more confinement to the soil. Fig. 12b shows that the average normal stress that acts on the compound sharp anchor does not saturate at 4 or 5 sharp blades. The normal stress on the 6-sharp anchor is close to the normal stress that acts upon the disk-shaped anchor of same convex hull (25.8 kPa), which suggests that saturation might be reached at 6 sharp blades. This hypothesis is corroborated by the granular flow visualizations in Section 6.2.

## 6.2. Granular flow and arching effects

We expected that important changes in granular flow direction would occur when the anchor blades transition from an independent to a cooperative response. For fan-shaped compound anchors, this transition occurs between 3 and 4 blades. Fig. 13 shows the velocity profiles of SPH particles during the intrusion of 1-fan, 3-fan, 4-fan anchors, which exhibit an independent, transitioning and cooperative response, respectively. The granular flow around the disk-shaped anchor is also shown for reference. For a single-blade anchor, the soil mass that moves with the anchor as a pseudo-rigid body is shaped like a wedge, the downward granular flow below the anchor is quasi vertical (the deviation angle  $\theta$  is around  $5^\circ$ ), and the upward granular flow around the anchor is also close to the vertical, which means that the 1-fan anchor tends to “cut through” the soil, in a similar way as a strip foundation would. For the 4-fan and disk anchors, the mass of soil that moves with the anchor as a pseudo-rigid body is shaped like a cone (with non convex boundaries between the blades), the downward granular flow below the anchor is inclined at  $40^\circ$ , and the upward granular flow around the anchor departs from the vertical, especially at the periphery of the convex hull of the compound anchor, where the soil follows a radially outward trajectory. The response of a 3-fan anchor in intermediate between these two cases, with a downward vertical flow oriented at an angle of  $15^\circ$  under the blades.

Fig. 14 is a snapshot of particle flow velocity profiles under the bottom face of 1-fan, 3-fan and 4-fan anchors at an intrusion an depth of 10 mm. Soil flows in a direction orthogonal to the 1-fan blade, whereas granular flow is directed radially outward around the 4-fan anchor, because the orthoradial flow is impeded by the adjacent blades, which apply an extra confinement to the soil under the anchor. Granular flow under the convex hull of a 4-fan anchor is similar to that under a disk-shaped anchor. Granular flow around a 3-fan anchor presents features of both the 1-fan and 4-fan anchors, which confirms that the response of the 3-fan compound anchor is a transition from a strip-like to a disk-like response.

Fig. 15 shows the velocity profiles between two blades of the 3-fan and 4-fan compound anchors in a vertical planes orthogonal to the radial direction. For the 4-fan anchor, a volume of soil moves as a pseudo-rigid block not only under the blades, but also in between, which corroborates the hypothesis of arching effects, whereby the locus of the maximum compression principal stress is an arch formed by adjacent elements that engage the soil underneath with compression stress and deformation. By contrast, the soil between the blades of the 3-fan anchor undergoes small velocities, which means that the mass of soil displaced is mostly under the blades as opposed to under the whole convex hull of the compound anchor. In other words, arching effects are likely insignificant between the blades of the 3-fan anchor at the location of the cut. The comparison of the 3-fan and 4-fan anchor systems thus explains the transition in the curves of anchor intrusion resistance and normal stress in Fig. 11.

Figs. 16 and 17 show the velocity profiles of SPH particles during the intrusion of 1-sharp, 3-sharp and 6-sharp anchors. The velocity field around the 1-sharp anchor is similar to that around the 1-fan anchor: the soil moves as a pseudo-rigid wedge under the blade with little deviation from the vertical, and the soil around the blade moves upward following a quasi-perfect vertical trajectory, indicating that the sharp blade is “cutting through” the soil mass. A radially outward granular flow is observed under each blade of the 6-sharp anchor,

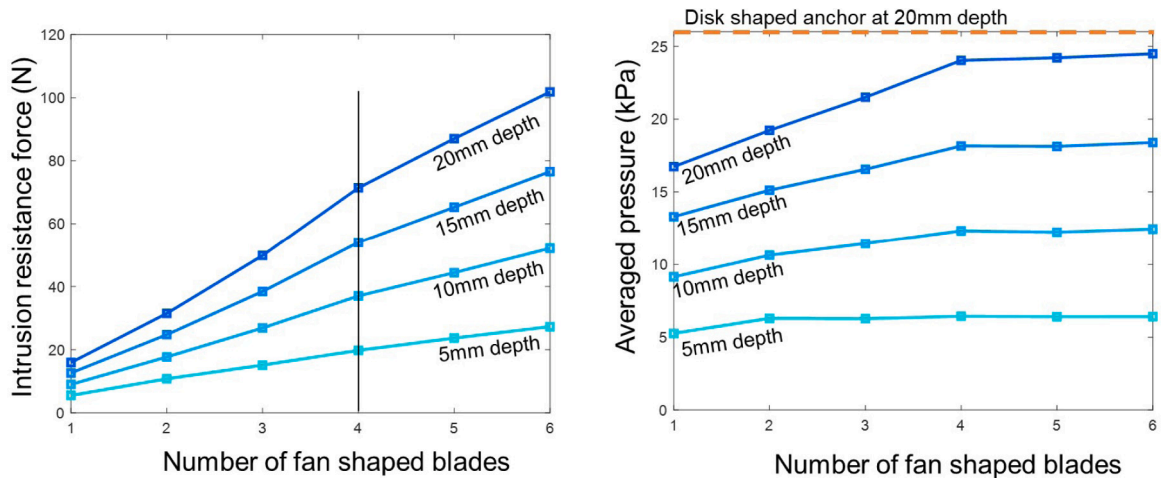


Fig. 11. Anchoring force and averaged normal stress on the bottom face of fan-shaped anchor systems at depths of 5 mm, 10 mm, 15 mm, and 20 mm (experimental results).

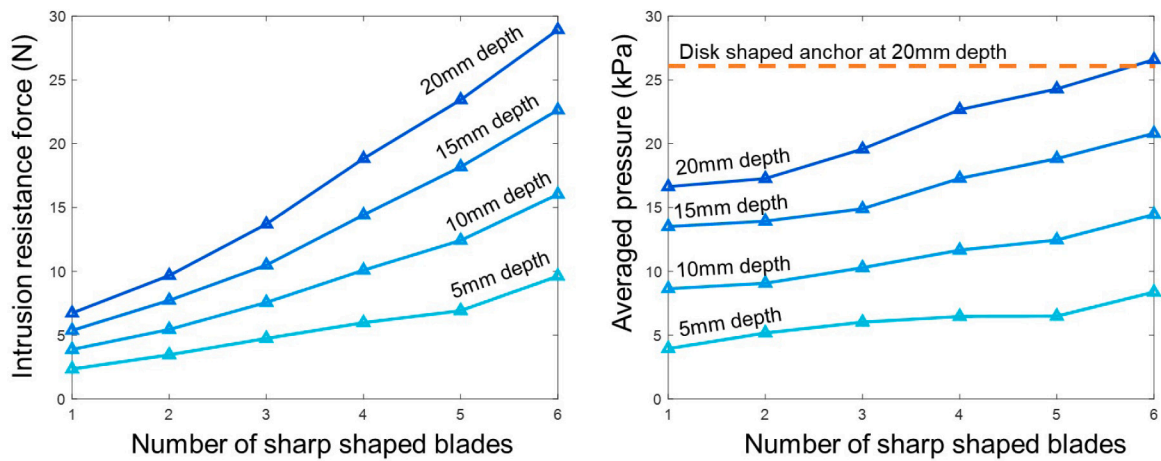


Fig. 12. Anchoring force and averaged normal stress on the bottom face of sharp-shaped anchor systems at depths of 5 mm, 10 mm, 15 mm, and 20 mm (experimental results).

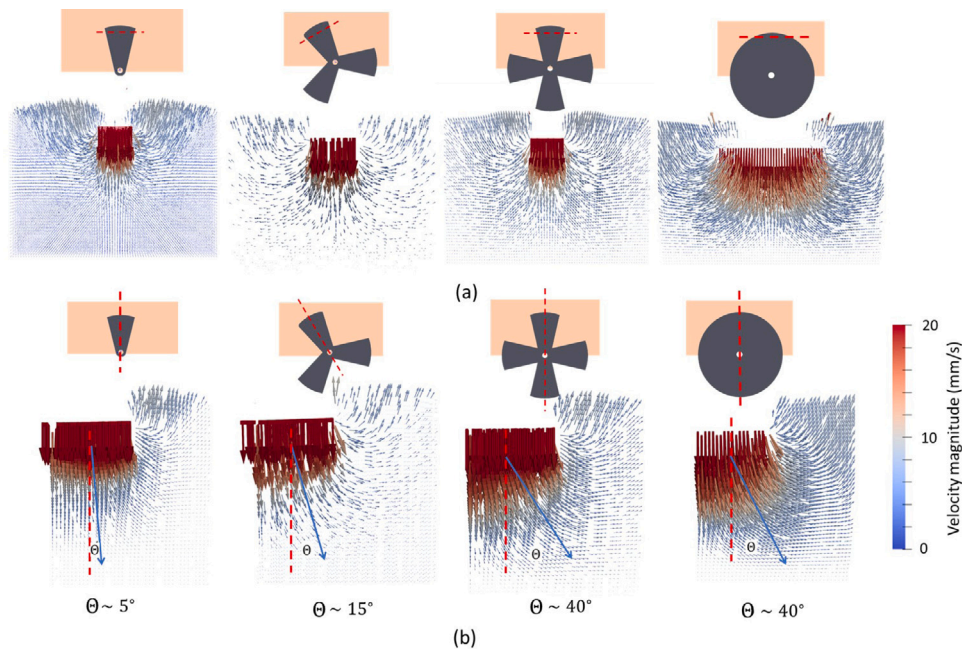


Fig. 13. Velocity field in the soil intruded by 1-fan, 3-fan, 4-fan and disk anchors. The plots were extracted from simulation results for an intrusion depth of 10 mm. The plots are vertical cross-sectional views of the numerical model. The position of the cross-cutting plane where the velocity field is plotted is marked by a red dashed line in the sketches. The blue arrows indicate the direction of the granular flow, which is oriented at an angle  $\theta$  from the vertical. (a) Orthoradial cut. (b) Radial cut.

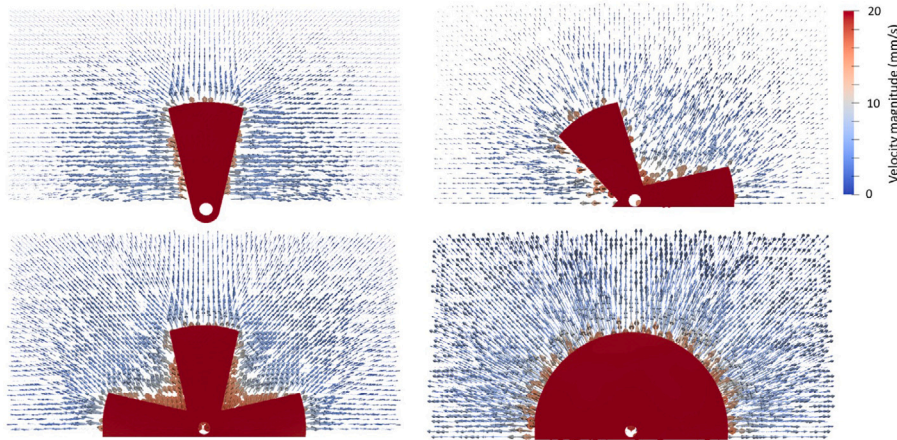


Fig. 14. The horizontal velocity field of SPH particles under the bottom face of 1-fan, 3-fan, 4-fan and disk anchors at an intrusion depth of 10 mm (simulation results).

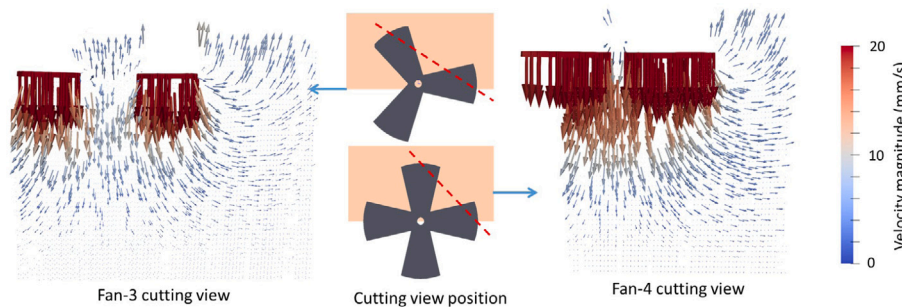


Fig. 15. The granular flow profile between adjacent blades for 3-fan and 4-fan compound anchor systems at an intrusion depth of 10 mm (simulation results).

which can be explained by the extra confinement provided by the adjacent blades, which limits the orthoradial flow. The volume of soil displaced by each blade of the 6-sharp compound anchor is larger than that displaced by a single sharp anchor, which explains the increase of the normal stress on the anchor with the number of blades in Fig. 12.b. The quasi-absence of orthoradial flow around the 6-sharp compound anchor suggests that arching mechanisms are fully active and that the normal stress on the 6-sharp anchors reached saturation. The response of a 3-sharp anchor exhibits features of the two end cases (1-sharp, 6-sharp), where the orthoradial flow pattern deviates from that around the single sharp blade because of the confinement created by the adjacent blades.

### 6.3. Soil volumetric deformation and failure mechanisms

Figs. 18 and 19 respectively show the distributions of compressive volumetric strain and shear strain rates at intrusion depths of 2 mm, 5 mm and 10 mm. The plots are vertical orthoradial cross-sectional views of the numerical models of 1-fan, 4-fan, 1-sharp and 4-sharp anchor models. The 4-fan anchor model is observed under one blade, while the 4-sharp model is observed between two blades.

Directly under the 1-fan blade, a volume of compressed soil with a bulb-shaped profile forms (Fig. 18 first row). The size of that bulb increases with the intrusion depth but the maximum value reached by the compressive volumetric strain in that volume (5% in this case) is the same for all three intrusion depths. The soil around the compressed zone is pushed away and diverted towards the free surface, which results in the formation of triangular profile zones that slide on each side of the 1-fan anchor. Similar phenomena are observed under the 1-sharp anchor (Fig. 18 third row), but the bulb-shaped compressed zone under the blade is narrower and the magnitude of the compressive strain in the triangular sliding zones is smaller. The zone of compressed

soil under a blade of the 4-fan anchor (Fig. 18 second row) is similar to, but larger than that under the blade of the 1-fan anchor. Additionally, the maximum compressive volumetric strain is lower under one of the blades of the 4-fan anchor than under a single fan-shaped anchor. These observations demonstrate the effect of the extra confinement from the adjacent blades and illustrate probable arching mechanisms, which tend to distribute soil deformation when anchor blades “cooperate”, i.e., interact. Since a larger mass of soil is mobilized under a 4-fan anchor than under a single fan-shaped anchor, the normal stress on the 4-fan anchor is larger than that on the 1-fan anchor (Fig. 11). The side view of the 4-sharp anchor shows that the compressive strain is close to zero except in a localized zone shaped like an arch as a consequence of stress redistribution, which confirms the occurrence of arching. An arch of compressed soil between the blades forms at low penetration depth (2 mm) and pushes the soil below it when the anchor is at larger penetration depths (5 mm and 10 mm). The triangular sliding zones are not visible between two sharp blades in Fig. 18. This is because arching and subsequent changes in penetration resistance can only occur when the distance between two blades is within a range that depends on the grain size, as previously noted in Cruz and Caballero-Robledo (2016), Pravin et al. (2021) and Agarwal et al. (2021). The distance between end points of two adjacent blades has visibly exceeded that threshold in the 4-sharp anchor system. Overall, the multi-blade anchors distribute compressive volumetric strains, mobilize a larger volume of soil than their blades acting independently, and are thus subjected to a larger normal stress. Our interpretation is that arching develops between blades close to the anchor centroid and not close to the end points of the blades for 4-sharp anchors. We propose that arching is fully active when the end points of the blades of the compound anchor are separated by a distance that is below a critical length that depends on the grain size, in which case, the compound anchor is “saturated” and the normal stress on the anchors at a given depth ceases to increase with the number

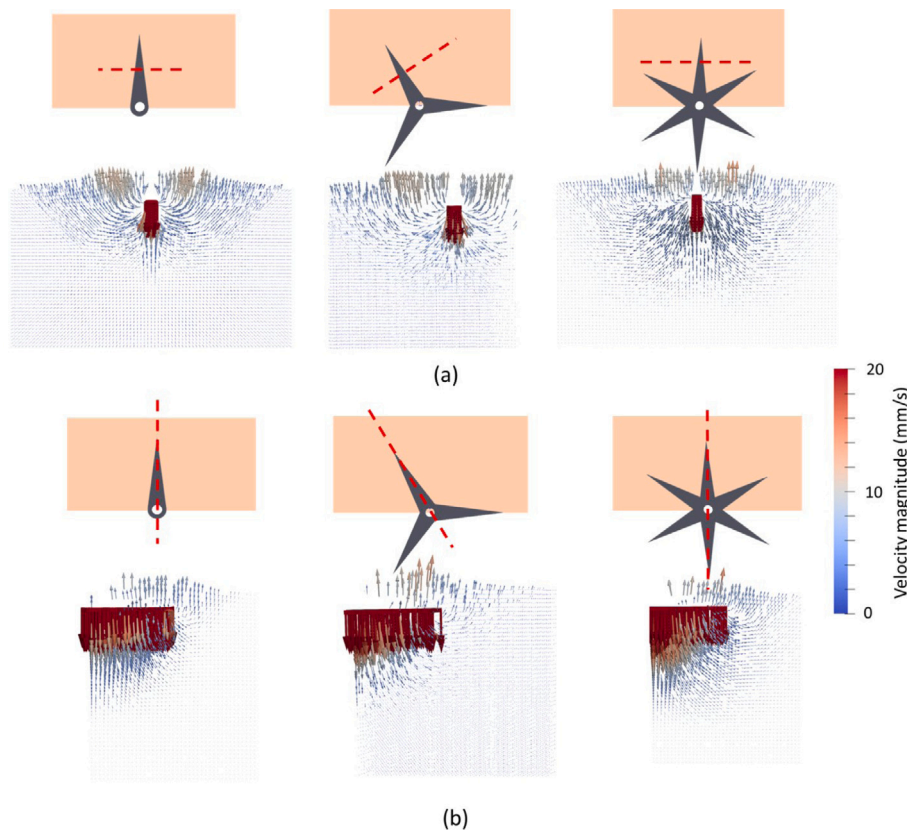


**Fig. 16.** Velocity field in the soil intruded by 1-sharp, 3-sharp and 6-sharp anchors. The plots were extracted from simulation results for an intrusion depth of 10 mm. The plots are vertical cross-sectional views of the numerical model. The position of the cross-cutting plane where the velocity field is plotted is marked by a red dashed line in the sketches. (a) Orthoradial cut. (b) Radial cut.

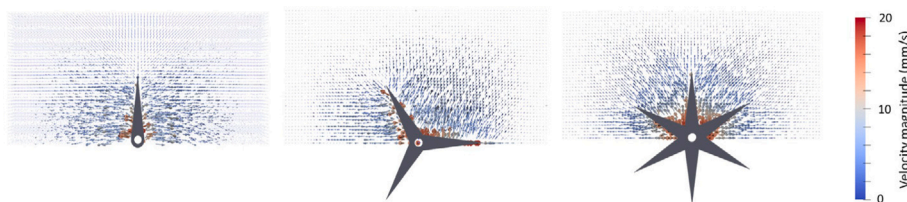


**Fig. 17.** The horizontal velocity field of SPH particles under the bottom face of 1-sharp, 3-sharp and 6-sharp anchors at an intrusion depth of 10 mm (simulation results).

of blades. This saturation occurs between 3 and 4 blades for the fan-shaped anchors and at 6 blades for the spike-shaped anchors (note that rigorously speaking, another test with at least 7 sharp blades is needed to confirm saturation at 6 sharp blades).

Fig. 19 shows that the bulb-shaped zone of compressed soil below the 1-fan anchor is not fully rigid. It is composed of a small rigid triangular wedge (that undergoes a constant shear strain) and a sheared zone beyond that wedge. The wedge acts as an intruding front. The localized shear strains in line with the edges of the 1-fan anchor suggests that the soil that is in the compressed zone beyond the wedge is sliding and continuously being replaced. The triangular sliding zones on the sides of the 1-fan model are visible in Fig. 19 (first row). Our hypothesis is that the shearing rate increases along the slipping planes up to shear failure, at which point, the triangular zones slide on the slipping planes as pseudo-rigid bodies. The shearing rate increases in localized zones around the slipping planes as the intrusion depth increases. The formation of the triangular sliding zones close to the end points of a blade of the 4-fan anchor is impeded by the extra confinement exerted by the adjacent blades, which prevents the soil from flowing towards the free surface. Interestingly, the blade of the 1-sharp anchor is surrounded by two parallel triangular zones delimited

by a higher shear strain rate. This suggests that two sliding mechanisms occur concurrently, with one pseudo-rigid body sliding in another. For the 4-sharp anchor (Fig. 19, fourth row), the sliding surfaces of the two individual spike-shaped anchors (shown in Fig. 19, third row) merge into a single failure surface. The soil between blades can no longer flow towards the free surface because the shearing surface is intercepted by the shearing surface of one of the two adjacent blades. Similarly, the sheared zone of the individual fan-shaped blades is disturbed by the presence of adjacent blades. Although the view shown in Fig. 19 (fourth row) does not highlight failure mechanisms merging, the distribution of the shear strain rate suggests arching effects, i.e. the transfer of stress from a moving soil mass to an adjacent stationary soil mass.

### 7. Conclusions

A robust approach to couple the FEM and SPH was implemented and applied to simulate the intrusion of deformable compound anchors in dry slightly polydisperse silica sand. To the authors' knowledge, this is the first time that a granular medium is modeled by SPH in the domain of large deformations and FEM in the far field. In previous FEM + SPH models such as those used for simulating metal cutting, the FEM and

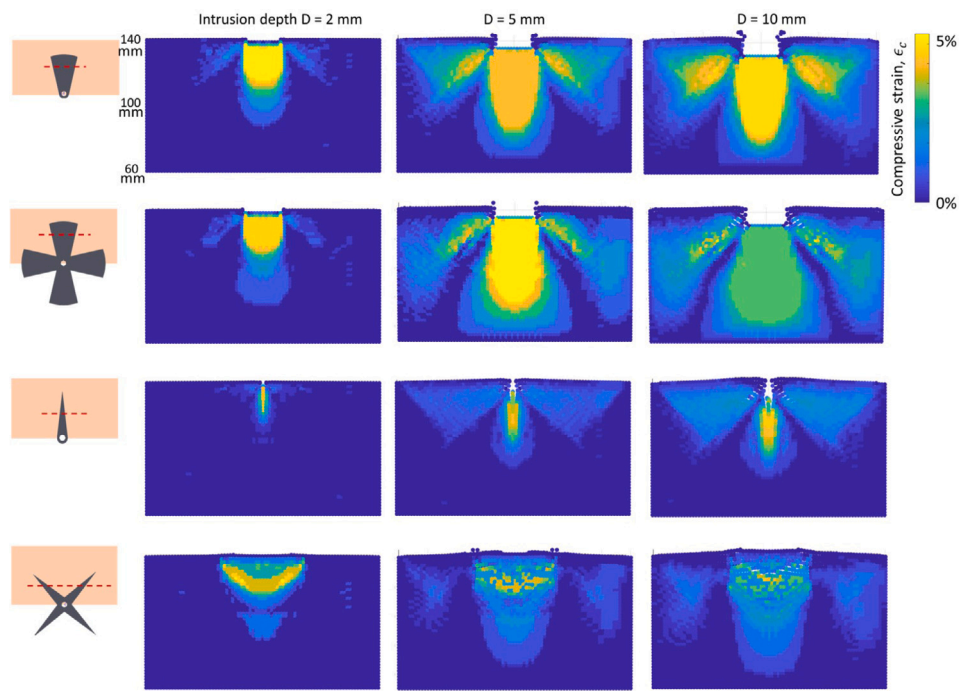


Fig. 18. Compressive strain fields in the SPH soil domain at an intrusion depth of 2 mm, 5 mm and 10 mm for 1-fan, 4-fan, 1-sharp and 4-sharp anchor models. The plots are vertical cross-sectional views of the numerical model. The position of the cross-cutting plane where the velocity field is plotted is marked by a red dashed line in the sketches.

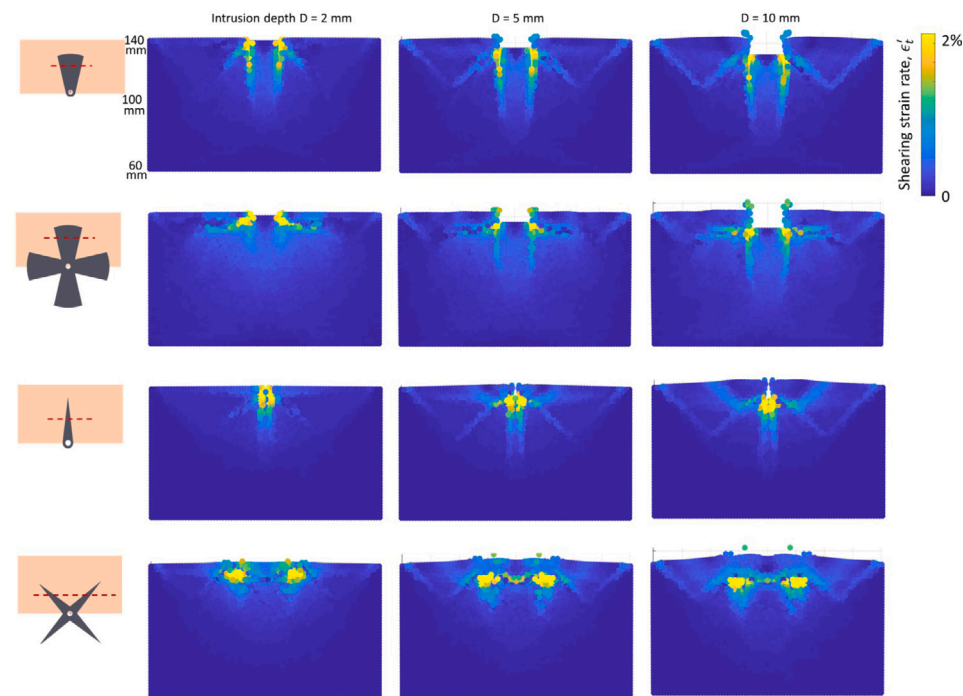


Fig. 19. Shear strain rate fields in the SPH soil domain at an intrusion depth of 2 mm, 5 mm and 10 mm for 1-fan, 4-fan, 1-sharp and 4-sharp anchor models. The plots are vertical cross-sectional views of the numerical model. The position of the cross-cutting plane where the velocity field is plotted is marked by a red dashed line in the sketches.

SPH were not applied simultaneously to the same material as a single unit, and yet, the connectivity between the FEM and SPH domains was represented by perfect ties (i.e., shared nodes). In the approach proposed here, the two domains interact through reaction forces calculated based upon a realistic soil constitutive model. The programs developed in this study allowed automatic pre-and post-processing and facilitated the use of open-source tools to visualize the computation

results obtained with LS-DYNA, hence creating a user-friendly interface — a significant advantage over some of the particulate mechanics software available in the public domain.

The simulations showed good agreement with experimental force-displacement curves for penetration depths of 8 mm or more (respectively, 20 mm or more) for spike-shaped (respectively, fan-shaped)

anchors with 1 to 6 blades. Analyses of granular flow and volumetric deformation highlighted that when the angular distance between anchor components is below a certain threshold, the intrusion force stems from the reaction of the soil not only below the blades, but also, between the blades. We attribute this “anchor cooperation” to 3D arching effects. Arching effects, i.e., the transfer of stress from a slipping soil mass to an adjacent stationary soil mass, did not translate into a significant gain of intrusion resistance for sharp blades. For fan-shaped anchors, it was found that the average normal stress that acts on the anchor saturates to a plateau value when anchors comprise at least four blades. For both fan-shaped and sharp anchor blades, the horizontal granular flow was orthogonal to the contour of the blades for 1 and 2 components, radial (outward) for 5 and 6 components and followed a transition regime for 3 or 4 components, from orthoradial to radially outward flow. A pseudo-rigid wedge of soil formed directly under the blades. The granular flow ahead of the wedge was quasi-vertical for single-blade anchors. The inclination angle of the granular flow below the wedge increased with the number of blades, to reach 40° for four fan-shaped blades and above. The 4-fan compound anchor was similar to a circular anchor of the same outer diameter both in terms of force–displacement curve and granular flow patterns.

The multi-blade anchors distribute compressive volumetric strains, mobilize a larger volume of soil than their blades acting independently, and are thus subjected to a larger normal stress. Arching mechanisms develop between blades when they are separated by a distance that does not exceed a critical length. A greater number of blades reduces the angular distance between the blades and enables arching on a larger portion of the blade length, from the centroid of the compound anchor outward. We posit that arching is fully active when the angular distance between end points of the blades of the compound anchor is smaller than the critical length, in which case, the compound anchor is “saturated” and the normal stress that acts on the anchors at a given depth ceases to increase with the number of blades. This saturation occurs between 3 and 4 blades for the fan-shaped anchors and likely at 6 blades for the spike-shaped anchors (although at least one test with more than 6 spike-shaped anchors would be necessary to confirm this statement). The distribution of shear strain highlights a failure mechanism reminiscent of Prandtl’s foundation sliding model for single-blade anchors. A rigid wedge of soil forms under the blades and acts as an intruder. The soil mass under it is compressed uniformly but does not act as a rigid body, because it is traversed by localized shear bands in line with the edges of the blades. This is indicative of granular flow towards the free surface, on the sides of the blades. That granular flow is impeded by adjacent blades, which results in a complex failure mechanism that combines sliding and arching.

#### CRedit authorship contribution statement

**Haozhou He:** Conceptualization, Methodology (numerical simulations), Software (testing of existing code components), Validation (validation of the numerical models), Formal analysis, Investigation (simulations), Data curation (numerical results), Writing – original draft, Visualization. **Andras Karsai:** Conceptualization, Methodology (experimental protocol), Validation (reproducibility of the experimental tests), Formal analysis, Investigation (experiments), Data curation (experimental results), Writing – review & editing. **Bangyuan Liu:** Conceptualization, Investigation (experiments). **Frank L. Hammond III:** Conceptualization, Supervision, Funding acquisition. **Daniel I. Goldman:** Conceptualization, Methodology (experimental protocol), Validation (reproducibility of the experimental tests), Resources (materials and laboratory supplies, testing set-up), Writing – review & editing, Supervision, Funding acquisition. **Chloé Arson:** Conceptualization, Methodology (numerical simulations), Validation (validation of the numerical models), Formal analysis, Resources (computing resources), Writing – original draft, Supervision, Project administration, Funding acquisition (lead PI).

#### Declaration of competing interest

The authors declare that they have no known competing financial interests or personal relationships that could have appeared to influence the work reported in this paper.

#### Data availability

Data will be made available on request.

#### Acknowledgments

This material is based upon work primarily supported by the Engineering Research Center Program of the National Science Foundation, United States under NSF Cooperative Agreement Number EEC-1449501. Funding for this research was also provided by the National Science Foundation, United States under Grant No. 1935548, and by UKRI NERC, United States grant NE/T010983/1. Additional funding for Andras Karsai and Daniel I. Goldman was provided by the NASA Jet Propulsion Laboratory, United States under the JPL Sponsor Award Number 1671083. Any opinions, findings and conclusions, or recommendations expressed in this material are those of the author(s), and do not necessarily reflect those of the NSF or the NASA.

#### References

- Agarwal, S., Karsai, A., Goldman, D.I., Kamrin, K., 2021. Efficacy of simple continuum models for diverse granular intrusions. *Soft Matter* 17, 7196–7209.
- Agarwal, S., Senatore, C., Zhang, T., Kingsbury, M., Iagnemma, K., Goldman, D.I., Kamrin, K., 2019. Modeling of the interaction of rigid wheels with dry granular media. *J. Terramech.* 85 (2019), 1–14.
- Alejano, L.R., Bobet, A., 2012. Drucker–prager criterion. In: *The ISRM Suggested Methods for Rock Characterization, Testing and Monitoring: 2007–2014*. Springer, pp. 247–252.
- Beuth, L., 2012. Formulation and Application of a Quasi-Static Material Point Method (Ph.D. thesis). Institut für Geotechnik der Universität Stuttgart, Germany.
- Bhattacharya, P., Kumar, J., 2014. Vertical pullout capacity of horizontal anchor plates in the presence of seismic and seepage forces. *Geomech. Geoenviron. Eng.* 9 (4), 294–302.
- Bisht, V., Salgado, R., Prezzi, M., 2021. Material point method for cone penetration in clays. *J. Geotech. Geoenviron. Eng.* 147 (12), 04021158–1–16.
- de Bono, J.P., McDowell, G.R., 2022. Some important aspects of modelling clay platelet interactions using DEM. *Powder Technol.* 398, 117056.
- Braun, A., Wang, X., Petrosino, S., Cuomo, S., 2017. SPH propagation back-analysis of baishuihe landslide in south-western China. *Geoenviron. Disasters* 4 (2), 1–10.
- Bui, H., Fukagawa, R., Sako, K., Ohno, S., 2008a. Lagrangian meshfree particles method (SPH) for large deformation and failure flows of geomaterial using elasticplastic soil constitutive model. *Int. J. Numer. Anal. Methods Geomech.* 32, 1537–1570.
- Bui, H.H., Nguyen, G.D., 2021. Smoothed particle hydrodynamics (SPH) and its applications in geomechanics: From solid fracture to granular behaviour and multiphase flows in porous media. *Comput. Geotech.* 138 (104315).
- Butlanska, J., Arroyo, M., Gens, A., O’Sullivan, C., 2014. Multi-scale analysis of cone penetration test (CPT) in a virtual calibration chamber. *Can. Geotech. J.* 51 (1), 51–66.
- Calvetti, F., Nova, R., 2005. Micro-macro relationships from DEM simulated element and in-situ tests. In: *Proceedings of 5th International Conference of Micromechanics of Granular Media: Powders and Grains 200*. pp. 245–250.
- Ceccato, F., Beuth, L., Simonini, P., 2017. Adhesive contact algorithm for MOM and its application to the simulation of cone penetration in clay. *Procedia Eng.* 175, 182–188.
- Chen, Y., Martinez, A., DeJong, J.T., 2022. DEM study of the alteration of the stress state in granular media around a bio-inspired probe. *Can. Geotech. J.* (ja).
- Coduto, D.P., Kitch, W.A., Yeung, M.-c.R., 2001. *Foundation Design: Principles and Practices*, Vol. 2. Prentice Hall, Upper Saddle River.
- Coetzee, C., Vermeer, P., Basson, A.H., 2005. The modelling of anchors using the material point method. *Int. J. Numer. Anal. Methods Geomech.* 29 (9), 879–895.
- Cruz, R.L.D.L., Caballero-Robledo, G., 2016. Lift on side-by-side intruders within a granular flow. *J. Fluid Mech.* 800, 248–263.
- Das, B., 1980. A procedure for estimation of ultimate uplift capacity of foundations in clay. *Soils Found.* 20, 77–82.
- Das, B.M., Larbi-Cherif, S., 1983. Bearing capacity of two closely-spaced shallow foundations on sand. *Soils Found.* 23 (1), 1–7.
- Domínguez, J., Crespo, A., Gómez-Gesteira, M., Marongiu, J., 2011. Neighbour lists in smoothed particle hydrodynamics. *Internat. J. Numer. Methods Fluids* 67 (12), 2026–2042.

- Evans, T.M., Zhang, N., 2019. Three-dimensional simulations of plate anchor pullout in granular materials. *Int. J. Geomech.* 19 (4), 04019004–1.
- Feng, Y., Blumenfeld, R., Liu, C., 2019b. Support of modified Archimedes' law theory in granular media. *Soft Matter* 15, 3008–3017.
- Feng, T., Xu, H., Song, J., Zhang, J., Zhou, M., Zhang, F., 2019a. Finite-element analysis of keying process of plate anchors in three-layer soft-stiff-soft clay deposits. *Adv. Civil Eng.* 2019.
- Fuller, M., 2010. The Application of Smooth Particle Hydrodynamics to the Modelling of Solid Materials (Ph.D. thesis). University of Leicester.
- Geddes, J., Murray, E., 1996. Plate anchor groups pulled vertically in sand. *J. Geotech. Eng. ASCE* 122, 509–516.
- Gens, A., Arroyo, M., Butlanska, J., O'Sullivan, C., 2018. Discrete simulation of cone penetration in granular materials. In: *Advances in Computational Plasticity. Computational Methods in Applied Sciences*, Vol. 46. pp. 95–111.
- Gingold, R., Monaghan, J., 1977. Smoothed particle hydrodynamics: theory and application to non-spherical stars. *Mon. Not. R. Astron. Soc.* 181 (3), 375–389.
- Gray, J.P., Monaghan, J.J., Swift, R.P., 2001. SPH elastic dynamics. *Comput. Methods Appl. Mech. Engrg.* (190), 6641–6662.
- Hakeem, N.A., Aubeny, C., 2019. Numerical investigation of uplift behavior of circular plate anchors in uniform sand. *J. Geotech. Environ. Eng.* 145 (9).
- Hanna, T., Sparks, R., Yilmaz, M., 1972. Anchor behaviour in sand. *J. Soil Mech. Found. Div. ASCE* 98, 1187–1207.
- Hosoi, A., Goldman, D.I., 2015. Beneath our feet: strategies for locomotion in granular media. *Annu. Rev. Fluid Mech.* 47, 431–453.
- Huang, W., Sheng, D., Sloan, S., Yu, H., 2004. Finite element analysis of cone penetration in cohesionless soil. *Comput. Geotech.* 31 (7), 517–528.
- Isava, M., et al., 2016. Razor clam-inspired burrowing in dry soil. *Int. J. Non-Linear Mech.* 81, 30–39.
- Jonak, J., Siegmund, M., Karpinski, R., Wojcik, A., 2020. Three-dimensional finite element analysis of the undercut anchor group effect in rock cone failure. *Materials* 13 (6), 1332–1349.
- Khatri, V., Kumar, J., 2009. Vertical uplift resistance of circular plate anchors in clays under undrained condition. *Comput. Geotech.* 36 (8).
- Khosravi, A., Martinez, A., DeJong, J., 2019. Discrete element model (DEM) simulations of cone penetration test (CPT) measurements and soil classification. *Can. Geotech. J.* 57, 1369–1387.
- Kitamoto, H., Omori, H., Nagai, H., Nakamura, T., Osumi, H., Kubota, T., 2012. Development of a propulsion mechanism for a lunar subsurface excavation robot with peristaltic crawling mechanism. In: *Proc. Int. Symposium on Artificial Intelligence, Robot. and Autom. in Space*.
- Korzani, M.G., Galindo-Torres, S.A., Scheuermann, A., Williams, D.J., 2017. Parametric study on smoothed particle hydrodynamics for accurate determination of drag coefficient for a circular cylinder. *Water Sci. Eng.* 10 (2), 143–153.
- Kouzer, K.M., Kumar, J., 2009a. Vertical uplift capacity of equally spaced horizontal strip anchors in sand. *Int. J. Geomech.* 9, 230–236.
- Kouzer, K.M., Kumar, J., 2009b. Vertical uplift capacity of two interfering horizontal anchors in sand using an upper bound limit analysis. *Comput. Geotech.* 36, 1084–1089.
- Kulak, R.F., Bojanowski, C., 2011. Modeling of cone penetration test using SPH and MM-ALE approaches. In: *Proc. 8th European LS-DYNA Users Conference*. pp. 1–10.
- Kulak, R.F., Schwer, L., 2012. Effect of soil material models on SPH simulation for soil-structure interaction. In: *Proc. 12th International LS-DYNA Users Conference*. pp. 1–9.
- Kumar, J., Kouzer, K., 2008. Vertical uplift capacity of horizontal anchors using upper bound limit analysis and finite elements. *Can. Geotech. J.* 45, 698–704.
- Liang, W., Zhao, J., Wu, H., Soga, K., 2021. Multiscale modeling of anchor pullout in sand. *J. Geotech. Geoenviron. Eng.* 147 (9), 04021091–1.
- Libersky, L.D., Randles, P.W., Carney, T.C., Dickinson, D.L., 1997. Recent improvements in SPH modeling of hypervelocity impact. *Int. J. Impact Eng.* 20, 525–532.
- Liyanapathirana, D., 2009. Arbitrary Lagrangian Eulerian based finite element analysis of cone penetration in soft clay. *Comput. Geotech.* 36, 851–860.
- Lu, C., Sonoda, Y., 2021. An analytical study on the pull-out strength of anchor bolts embedded in concrete members by SPH method. *Appl. Sci.* 11 (18), 727–731.
- Ma, Y., Evans, T.M., Cortes, D.D., 2020. 2D DEM analysis of the interactions between bio-inspired geo-probe and soil during inflation–deflation cycles. *Granul. Matter* 22 (1), 1–14.
- Mallett, S.D., 2019. Mechanical Behavior of Fibrous Root-Inspired Anchorage Systems (Ph.D. thesis). Georgia Institute of Technology.
- Martinelli, M., Galavi, V., 2021. Investigation of the material point method in the simulation of cone penetration tests in dry sand. *Comput. Geotech.* 130 (103923), 1–15.
- Martinez, A., DeJong, J., Akin, I., Aleali, A., Arson, C., Atkinson, J., Bandini, P., Baser, T., Borela, R., Boulanger, R., et al., 2021. Bio-inspired geotechnical engineering: Principles, current work, opportunities and challenges. *Géotechnique* 1–19.
- Merfield, R.S., Lyamin, A.V., Sloan, S.W., 2005. Stability of inclined strip anchors in purely cohesive soil. *J. Geotech. Geoenviron. Eng.* 131 (6).
- Merfield, R.S., Sloan, S.W., 2006. The ultimate pullout capacity of anchors in frictional soils. *Can. Geotech.* 43 (8), 852–868.
- Merfield, R., Sloan, S., Yu, H., 2001. Stability of plate anchors in undrained clay. *Géotechnique* 52, 141–153.
- Monaghan, J., 1992. Smoothed particle hydrodynamics. *Annu. Rev. Astron. Astrophys.* 30 (1), 543–574.
- Monaghan, J., 2005a. Smoothed particle hydrodynamics. *Rep. Progr. Phys.* 68 (8), 1703–1759.
- Monaghan, J., 2005b. Theory and applications of smoothed particle hydrodynamics. *Front. Numer. Anal.* 143–194.
- Monaghan, J., 2012. Smoothed particle hydrodynamics and its diverse applications. *Annu. Rev. Fluid Mech.* 44 (44), 323–346.
- Murray, E., Geddes, J., 1987. Uplift of anchor plates in sand. *J. Geotech. Eng. ASCE* 113, 202–215.
- Naclerio, N.D., Karsai, A., Murray-Cooper, M., Ozkan-Aydin, Y., Aydin, E., Goldman, D.I., Hawkes, E.W., 2021. Controlling subterranean forces enables a fast, steerable, burrowing soft robot. *Science Robotics* 6 (55), eabe2922.
- Naderi-Boldaji, M., Alimardani, R., Hemmat, A., Sharifi, A., Keyhani, A., Tekeste, M.Z., Keller, T., 2012. 3D finite element simulation of a single-tip horizontal penetrometer–soil interaction. Part I: Development of the model and evaluation of the model parameters. *Soil Tillage Res.* 134, 153–162.
- Nagaoka, K., Kubota, T., Otsuki, M., Tanaka, S., 2010. Experimental analysis of a screw drilling mechanism for lunar robotic subsurface exploration. *Adv. Robot.* 24 (8–9), 1127–1147.
- Nonoyama, H., Moriguchi, S., Sawada, K., Yshima, A., 2015. Slope stability analysis using smoothed particle hydrodynamics (SPH) method. *Soils Found.* 55, 458–470.
- Ortiz, D., Gravish, N., Tolley, M.T., 2019. Soft robot actuation strategies for locomotion in granular substrates. *IEEE Robot. Autom. Lett.* 4 (3), 2630–2636.
- Pastor, M., Blanc, T., Haddad, B., Petrone, S., Morles, M.S., Drempevic, V., Issler, D., Crosta, G., Cascini, L., Sorbino, G., Cuomo, S., 2014. Application of a SPH depth-integrated model to landslide run-out analysis. *Landslides* 11, 793–812.
- Pravin, S., Chang, B., Han, E., London, L., Goldman, D.I., Jaeger, H.M., Hsieh, S.T., 2021. Effect of two parallel intruders on total work during granular penetrations. *Phys. Rev. E* 104 (2), 024902.
- Rowe, R., Davis, E., 1982. The behaviour of anchor plates in clay. *Géotechnique* 32, 9–23.
- Russell, R.A., 2011. CRABOT: A biomimetic burrowing robot designed for underground chemical source location. *Adv. Robot.* 25 (1–2), 119–134.
- Sano, H., Takahashi, A., Chiba, D., Hatta, T., Yamamoto, N., Itoi, E., 2013. Stress distribution inside bone after suture anchor insertion: simulation using a three-dimensional finite element method. *Knee Surg Sports Traumatol. Arthrosc.* 21 (8), 1777–1782.
- Sasson, M., Chai, S., Beck, G., Jin, Y., Rafieshahraki, J., 2016. A comparison between smoothed-particle hydrodynamics and RANS volume of fluid method in modelling slamming. *J. Ocean Eng. Sci.* 1 (2), 119–128.
- Seo, H., Pelecanos, L., 2018. Finite element analysis of soil-structure interaction in soil anchor pull-out tests. In: *Proceedings of the 9th European Conference on Numerical Methods in Geotechnical Engineering*, Porto, Portugal, June.
- Shen, K., Zhang, Y., Wang, K., Wang, B., Zhao, X., 2018. Effect of partial drainage on the pullout behaviour of a suction bucket foundation. *Eur. J. Environ. Civ. Eng.* 36, 883–894.
- Song, Z., Hu, Y., Randolph, M., 2008. Numerical simulation of vertical pullout of plate anchors in clay. *J. Geotech. Geoenviron. Eng.* 134, 866–875.
- Tao, J.J., Huang, S., Tang, Y., 2020. SBOR: a minimalistic soft self-burrowing-out robot inspired by razor clams. *Bioinspiration Biomim.* 15 (5), 055003.
- Terzaghi, K., 1943. *Theoretical Soil Mechanics*. John Wiley & Sons Inc.
- Tezcan, S.S., Keceli, A., Ozdemir, Z., 2006. Allowable bearing capacity of shallow foundations based on shear wave velocity. *Geotech. Geol. Eng.* 24 (1), 203–218.
- Tian, Y., Gaudin, C., Cassidy, M.J., 2014. Improving plate anchor design with a keying flap. *J. Geotech. Geoenviron. Eng.* 140, 04014009–1–13.
- Vacondio, R., Altomare, C.C., Leffe, M.D., Hu, X., Touze, D.L., Lind, S., Marongiu, J.-C., Marrone, S., Rogers, B., Souto-Iglesias, A., 2020. Grand challenges for smoothed particle hydrodynamics numerical schemes. *Comput. Part. Mech.* 8, 575–588.
- Vriend, N.M., Mcelwaine, J.N., Keylock, C., Ash, M., 2013. On the internal flow velocity of snow avalanches. In: *AGU Fall Meeting Abstracts*, Vol. 40. pp. 727–731.
- Wang, D., Bienen, B., Nazem, M., Tian, Y., Zheng, J., Pucker, T., Randolph, M.F., 2015. Large deformation finite element analyses in geotechnical engineering. *Comput. Geotech.* 65, 104–114.
- Wang, D., Hu, Y., Randolph, M.F., 2010. Three-dimensional large deformation finite-element analysis of plate anchors in uniform clay. *J. Geotech. Geoenviron. Eng.* 136 (2).
- Winter, A., Deits, R., Dorsch, D., Slocum, A., Hosoi, A., et al., 2014. Razor clam to RoboClam: burrowing drag reduction mechanisms and their robotic adaptation. *Bioinspiration Biomim.* 9 (3), 036009.
- Woo, J., Kim, D., Na, W.-B., 2015. Anchor dragging analysis of rock-berm using smoothed particle hydrodynamics method. *Shock Vib.* 2015 (687623).
- Wu, Q., An, Y., Liu, Q., 2015. SPH-based simulations for slope failure considering soil-rock interaction. *Procedia Eng.* 102, 1842–1849.

- Wu, H., Njock, P.G.A., Chen, J., Shen, S., 2019. Numerical simulation of spudcan-soil interaction using an improved smoothed particle hydrodynamics (SPH) method. *Mar. Struct.* 66 (2019), 213–226.
- Yang, E., Bui, H., Sterck, H.D., Nguyen, G., Bouazza, A., 2020. A scalable parallel computing SPH framework for predictions of geophysical granular flows. *Comput. Geotech.* 121 (103474).
- Zhao, S., Bui, H.H., Lemiale, V., Nguyen, G.D., Darve, F., 2019. A generic approach to modelling flexible confined boundary conditions in SPH and its application. *Int. J. Numer. Anal. Methods Geomech.* 43, 1005–1031.
- Zhou, Z., O’Loughlin, C.D., White, D.J., Stanier, S.A., 2020. Improvements in plate anchor capacity due to cyclic and maintained loads combined with consolidation. *Géotechnique* 70, 732–749.